Topological phase transitions in group IV-VI semiconductors by phonons

Jinwoong Kim and Seung-Hoon Jhi*

Department of Physics, Pohang University of Science and Technology, Pohang 790-784, Republic of Korea

(Received 26 March 2015; revised manuscript received 18 August 2015; published 23 September 2015)

The topological insulator has an intriguing electronic structure in that it has nontrivial topology enforcing the helical Dirac fermionic states at interfaces to the band insulators. Protected by the time-reversal symmetry and finite band gaps in the bulk, the topology is immune to external nonmagnetic perturbations. One essential question is whether elementary excitations in solids like phonons can trigger a transition in the topological property of the electronic structures. Here we investigate the development of topological insulating phases in IV-VI compounds under dynamic lattice deformations using first-principles calculations. Unlike the static state of topological phases at equilibrium conditions, we show that nontrivial topological phases are induced in the compounds by the dynamic lattice deformations from selective phonon modes. Calculations of the time-reversal polarization show that the Z_2 invariant of the compounds is flipped by the selective phonon modes and that the compounds exhibit oscillating topological phases upon dynamic lattice deformations.

DOI: 10.1103/PhysRevB.92.125142 PACS number(s): 71.20.−b, 73.22.Gk, 73.43.Nq

I. INTRODUCTION

Discovery of three-dimensional topological insulator (TI) casts a new frame to classify solids [1–3]. When the time-reversal symmetry is preserved, insulators are classified as either TI or normal insulator (NI) according to their topological invariant Z_2 number [4–6]. Recently, another topological phase by the crystalline mirror symmetry, namely, topological crystalline insulator (TCI), has been incorporated in the classification [7–9]. Since the topological invariant cannot be changed without going through the energy-gap closing, TIs should develop conducting helical states at the surfaces or the interfaces to NIs. Because of the spin-momentum locking of the helical states, back-scattering-free transport is feasible along the surfaces or interfaces. In this respect, the TI surfaces can work as excellent conducting channels of spin-polarized currents, reserving great potentials in spintronics applications. In addition, TIs are also expected to serve as low-energy platforms to detect nonabelian statistic particles such as a Majorana fermion, which would realize quantum computation [10]. Manipulating topological phases by controlling materials parameters thus opens ways to explore intriguing phenomena as well as to develop TI-based electronic devices.

Many emerging phenomena in solids are explained by the notion of elementary excitations and their interactions. While topological phases are usually referred to as geometrical characteristics of electronic structures of solids at equilibrium conditions, it is also of great physical interest to explore whether elementary excitations or interactions between them can lead to the development of topological phases or to new emerging phenomena associated with topological phases. PbTe, SnTe, and PbS, are narrow-gap semiconductors, and TCI phase is recently found in this group of compounds [8,11–14]. Interplay of crystalline symmetries and the time-reversal symmetry in these compounds leads to very rich behavior of topological phases. In this paper, we studied emerging topological phases in PbS, PbTe, and SnTe under lattice deformations by either static strains or dynamic phonon modes using first-principles calculations. We explore the crossover in topological phases between TCI, TI, and NI phases upon atomic displacements by strains, sound waves, or selective phonon modes. This paper provides an interesting demonstration that elementary excitations can induce nontrivial topological phases in narrow-gap semiconductors.

II. COMPUTATIONAL METHOD

First-principles calculations were carried out using Vienna *Ab initio* Simulation Package (VASP) [15,16]. The exchange correlation of electrons was treated within the generalized gradient approximation (GGA) as parameterized by Perdew, Burke, and Ernzerhof (PBE) [17]. Since band gaps calculated with GGA typically underestimate experimental values, we also used the screened hybrid-functional (HSE06) [18,19] to correct the band gaps (see below). The projector-augmented-wave (PAW) method [20,21] is used for atomic pseudopotentials, and the plane-wave basis is expanded up to a cutoff energy of 300 eV. The Brillouin zone is sampled with $8\times8\times8$ k-point grid for the bulk and $4\times4\times1$ k-point grid for the slab structures. In both cases, Γ point is included in the self-consistent calculations in order to properly take into account the effect of the band inversion at high-symmetry k-points. The spin-orbit interaction is included as implemented in the VASP code. We chose the parity-check scheme proposed by Fu and Kane for the verification of the Z_2 class [22]. For surface-band calculations, anion (Te or S)-terminated slab structures are used with the structural parameters obtained in the bulk calculations. The slab is constructed to have 73 monoatomic layers along the [111] direction, and the dangling bonds at surfaces are passivated by hydrogen atoms. The thickness of the vacuum region is approximately equal to the thickness of 36 monoatomic layers for each case. The superlattice structure possessing topological semimetal (TS) and topological crystalline semimetal (TCS) phases consist of 72 monoatomic layers.

III. RESULTS

First, we studied the effect of lattice deformations by hydrostatic pressures and uniaxial strains. It has been known that isotropic compressive (tensile) strain induces band

*jhish@postech.ac.kr

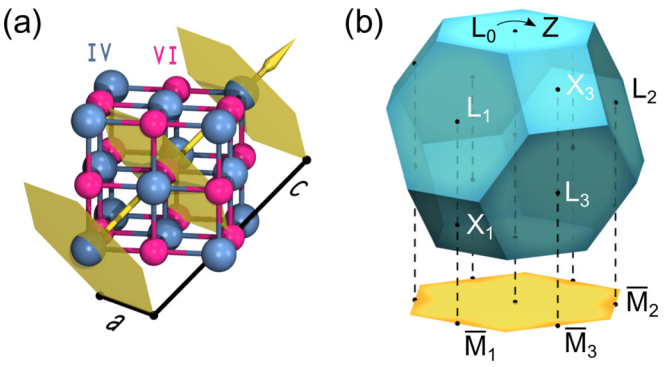

FIG. 1. (Color online) (a) Atomic structure of IV-VI compounds in the conventional unit cell. The lattice constants of the alternative hexagonal unit cell; (a) and (c) are denoted by solid lines. (b) The first Brillouin zones of fcc structure. The bottom shows the surface Brillouin zone projected onto the (111) plane.

inversion (restoration of band inversion) at four L points in PbTe(SnTe). The band inversion is recently reported to turn on the TCI phase. Uniaxial strains along the [111] direction [22] or chemical alloying [23] had been proposed to induce Z_2 nontrivial order in these compounds, which are needed to differentiate between equivalent four L points through breaking structural cubic symmetry. Therefore, combining both hydrostatic pressure and uniaxial strain would develop rich topological phases in these compounds. Figure 1(a) shows a conventional unit cell of group IV-VI semiconductors possessing rock salt structure, which is also considered as a hexagonal structure stacked along the [111] direction. Upon application of two types of strains, lattice constants a and c vary independently, and the L_0 point in the [111] direction turns into the Z point that is now distinguished from L_1, L_2, and L_3 points [Fig. 1(b)]. The Z_2 invariant was calculated from the parity at the time-reversal invariant momenta (TRIM) [22]. The parity is changed only by the band inversion at the TRIM, and the number of band inversion from the structural deformation determines the topological phase. Figure 2(c) shows the calculated topological phase diagram of PbS for varying lattice constants a and c. The direct band gap is finite in the whole region except the band inversion points, whereas the indirect-band gap is nonzero only in NI and TCI regimes. For example, deformation along p_h corresponds to hydrostatic pressure that deforms PbS to have the band inversion at four L points, inducing a topological phase transition from the NI to TCI phase. On the other hand, deformation along p_a (radial compressive strain) causes the band inversion at three L points, which leads to the TS phase, a nontrivial Z_2 order. Also, uniaxial compressive strain along the [111] direction [line p_c in Fig. 2(c)] causes the band inversion at Z and L point sequentially. PbTe and SnTe also has similar phase diagram.

The exchange-correlation functionals affect the estimation of transition point. For PbTe, the hydrostatic pressure for the band inversion is calculated with GGA to be about 1.6 GPa, which is smaller than experimental values of about $2.6 \sim 4$ GPa [24]. This is due to the well-known syndrome of band-gap underestimation of GGA. In order to correct the band-gap underestimation and subsequent error in the threshold stress, we repeated the calculations using the HSE06 hybrid functional, including Pb-d orbits as valence states with monotonously compressed volumes, following previously reported constraints to reproduce the proper band gap [25]. With corrected band gaps, the hydrostatic pressure at which the band inversion occurs is now estimated to be 3.87 GPa, in good agreement with experiment. For the threshold uniaxial strain at which PbTe has a nontrivial topological phase, GGA calculations give about $4.5\%(c/c_{\rm eq} = 0.955)$ or a stress of 0.54 GPa from the formula $(\partial E/\partial c)/a^2$ that converts the strain to the stress. The hybrid-functional correction enlarges the

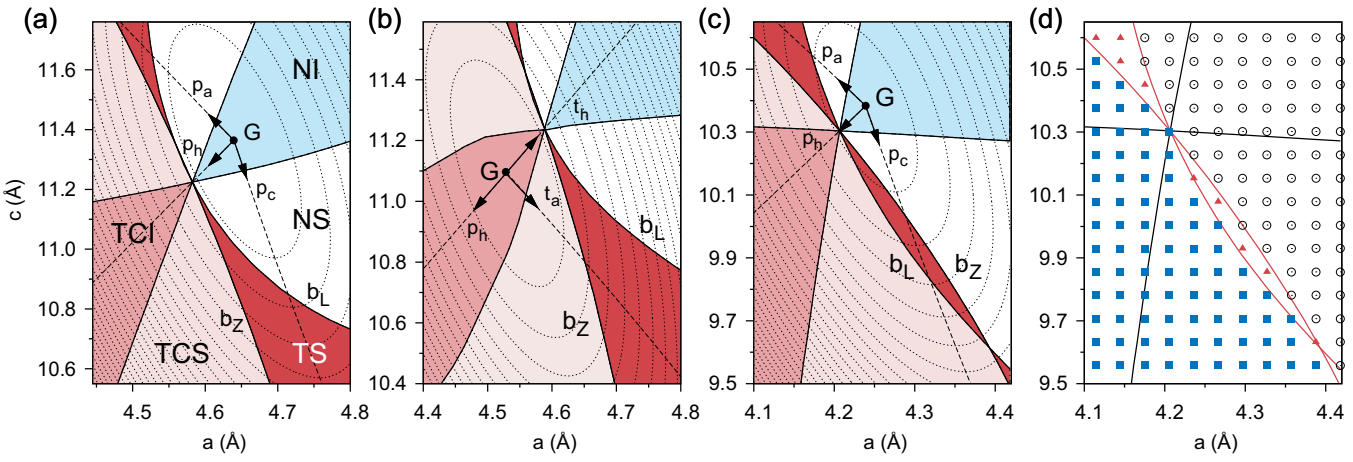

FIG. 2. (Color online) Calculated phase diagram upon lattice deformations. NI, normal insulator; NS, normal semimetal; TS, topological semimetal; TCS, topological crystalline semimetal; TCI, topological crystalline insulator. (a) PbTe, (b) SnTe, and (c), (d) PbS. Energy contours in dotted lines with G representing the equilibrium lattice constants. The solid lines b_L and b_Z denote the lattice parameters having the band inversion (or the parity change) at L and Z points, respectively. The direct band gap is finite in the whole range of a and c, but the indirect-band gap is nonzero only in NI (blue) and TCI (pale red) regimes. Deformation paths are denoted by dashed lines labeled as $X_Y(X = \{p,t\}; Y = \{h,c,a\})$, where X is for either compressive (p) or tensile (t) strain and Y is for the hydrostatic pressure (h), the uniaxial strain along the c axis (c), or the radial strain perpendicular to the c axis (a) [for instance, t_a corresponds to the stretching of the (111) plane]. (d) Phase diagram of PbS with calculated parity states (circle, normal phase; triangle, Z_2 nontrivial phase; rectangular, TCI nontrivial phase).

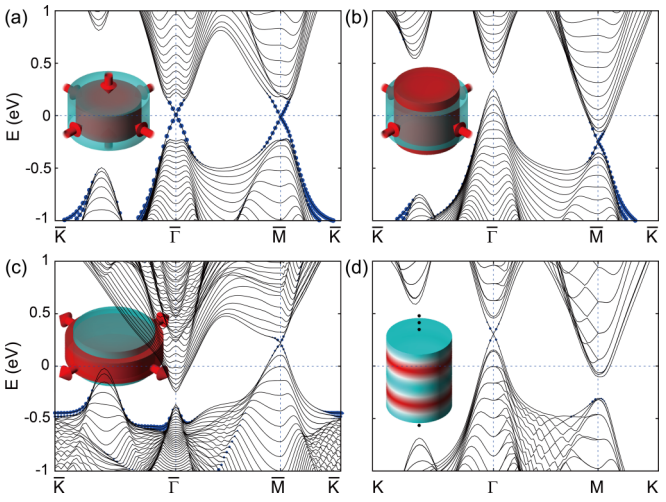

FIG. 3. (Color online) Calculated surface band structures at (111) surface for strained PbS (a) in TCI and (b) in TS phase. The inset illustrates the applied strains of (a) hydrostatic pressure and (b) radial compressive strain. (c) Topological surface state of SnTe possessing TS phase under radial tensile strain. The dots represent the states originating mostly from the surface atoms. (d) Topological bound state emerging at the domain boundary of TS-TCS phase superlattice, which is produced in PbS by applying sinusodially modulated strain (the inset).

band gap in all ranges of strain but gives the same feature of the band inversion at L point and steady gap size at Z point as GGA. The HSE06 correction gives the uniaxial stress of about 0.89 GPa to induce the topological phase. We note that the HSE06 correction does not change the tendency of the band gap variation upon the atomic displacement, and the phase diagrams within GGA are valid except for the underestimation of threshold strains.

Corresponding surface band structures in Figs. 3(a) and 3(b) for TCI and TS phases, respectively, clearly demonstrate the emergence of four and three Dirac cones. Upon anisotropic strains, electron and hole pockets are developed, and the surface states by Z_2 nontrivial phase are always accompanied by a bulk conducting state, as shown in Fig. 3(b). For SnTe, radial tensile strain restores a band inversion at Z point with retaining three band inversions so that the Z_2 nontrivial phase is induced instead of the TCI phase. Surface band structure of SnTe under radial tensile strain in Fig. 3(c) possesses only three Dirac cones, verifying the topological phase transition to the Z_2 nontrivial phase. Not only topological surface states emerge at interfaces to the NI region, but also they should exist at the boundary between TS and TCS phases. Figure 3(d) shows the bulk band structure of TS-TCS superlattice, which is produced by straining the c axis in a sinusoidal way. Upon such strain modulation, half of the structure can be in TS phase and the other half in TCS phase. We expect three and four Dirac cones in the (111) plane from TS and TCS phase regions, respectively. In fact, only one Dirac cone remains at Γ point after the topological charge neutralization [26]. A single difference between TS and TCS regions is the structural compression ratio along the [111] direction, and the spatial modulation of strains is in effect equivalent to longitudinal acoustic (LA) phonons. Phonon-induced strains are thus expected to lead different topological phases along the phonon-propagation direction, producing bulk Dirac cones. The group IV-VI compounds, in particular near critical strains to induce band inversions as illustrated in Fig. 2, may develop spatially modulated topological domains by acoustic phonon mode excitations.

We consider the dynamic lattice deformation by phonon modes. The atomic displacements of particular phonon modes that cause the parity reversal in the same way as the strains are of particular interest. If the parity reversal leads to a change in the topological invariant, we should observe nontrivial topological phases and the helical edge states for a short period of time within the adiabatic approximation. The validity of

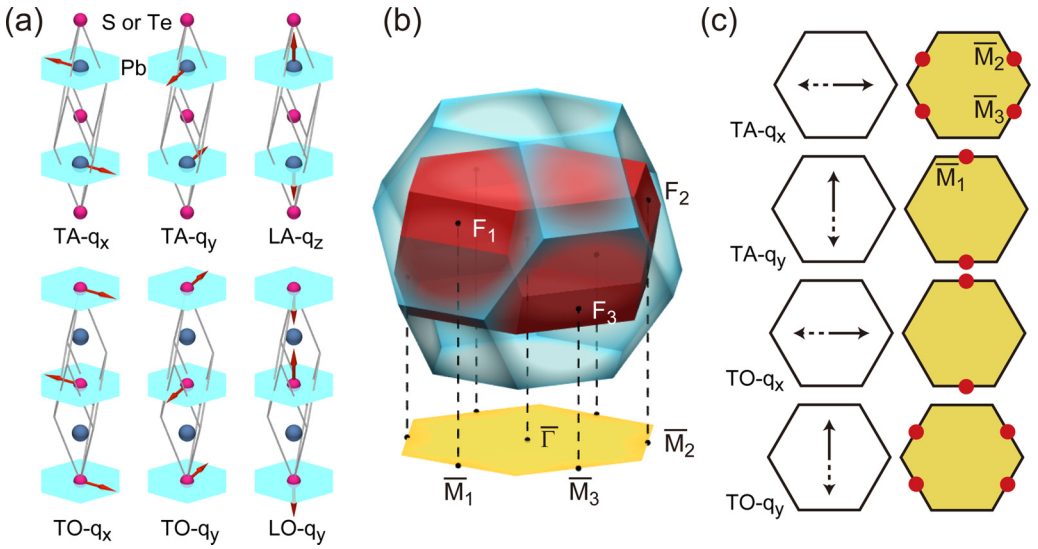

FIG. 4. (Color online) (a) Atomic displacements for all six phonon modes at L point. (b) The first Brillouin zones of fcc structure (in blue) and of its doubled structure (in red). (c) The atomic displacements for transverse modes (left panel) and the Dirac points in the (111) surface Brillouin zone (right panel) as denoted by the red dots. The Dirac cone is formed in a direction parallel (perpendicular) to the atomic displacement of the TA (TO) mode.

this approximation in evaluating the topological invariants is supported by successful reproduction via ensemble average of the renormalized band gap by phonon excitations [27]. Beyond the adiabatic approximation, renormalization of the band gap by the electron-phonon self-energy can affect the topological phase transition, as discussed in the two-band Dirac model [28,29]. The effect of acoustic phonon modes at Γ point is equivalent to the strains considered above. We found that optical modes at Γ point increase the band gap without causing any topological phase transition. On the other hand, the phonon modes at L point, which double the unit cell along the [111] direction as shown in Fig. 4(a), can induce intriguing topological phase transitions. We calculated the band gap at Γ and F points [projection of four L points in the original unit cell, as shown in Fig. 4(b)] and the band inversion by the ionic displacements corresponding to the phonon modes.

Figure 5 shows our calculated results for PbS. For longitudinal optical (LO) mode, the band gap at F point decreases as the atomic displacement is increased, and then the Z_2 TI phase is induced by the band inversion. For the LA mode, the band inversion at F point is followed by the one at Γ point, causing additional topological phase transition to TCI phase. In the case of the transverse modes (transverse acoustic (TA) and transverse optical (TO) modes), two independent (orthogonal) displacements should be considered because the modes are doubly degenerate. Upon ionic displacements, three equivalent F points are now distinguished by the subscript because the threefold degeneracy is removed. The direct band gaps at Γ and three F points are shown in Figs. 5(a) and 5(b) upon the atomic displacements corresponding to the transverse mode. Z_2 topological phases appear if the parity at one of the F points differs from those at other two F points. When the ionic displacements corresponding to TA-q_y or TO-q_x modes [Fig. 4(a)] are large enough to induce the band inversion, only the F_1 point has the opposite parity among TRIM, and thus a nontrivial topological phase is induced in PbS. Because the band gap reopens after the band inversion, PbS is in fact topological insulating and not semimetallic at such a moment [Figs. 5(e) and 5(f)]. If the amplitude of either TA-q_x or TO-q_y mode is sufficiently large, both F_2 and F_3 points change their parity as to result in the weak topological class [22] of 0;(011). Figure 6 shows the calculated phase diagram for PbTe by phonons.

In order to confirm explicitly the topological phase upon ionic displacements, we calculated surface band structures of PbS with ionic displacements of the TA phonon mode (Fig. 7). The F_i point in the bulk Brillouin zone is projected into the $\bar{M}_i$ point of the surface Brillouin zone. For the atomic displacement corresponding to TA-q_x mode [path d_1 in Fig. 5(e)], the band gaps at $\bar{M}_2$ and $\bar{M}_3$ points decrease as the atomic displacements are increased, as shown in Fig. 7(b). The Dirac cones are formed at $\bar{M}$ points when the displacement is larger than the threshold value of 0.5 Å (larger than for the bulk case due to the quantum confinement effect in the band gap). PbS becomes a weak TI for this atomic displacement while a strong topological order emerges with a single Dirac cone for the atomic displacement corresponding to TA-q_y mode (or its C_3 symmetric copies), as shown in Figs.7(d) and 7(e). On the other hand, for a circularly polarized TA phonon mode with ionic displacements along d_2 in Fig. 5(e), the band inversion occurs sequentially at F_3, F_2, and F_1 points, and the Dirac cones form at corresponding band-inversion $\bar{M}$ points, as illustrated in Fig. 7(f).

The surface Dirac-cone states are guaranteed to exist solely by the time-reversal symmetry because the structural mirror symmetries are broken by the ionic displacement except for the case of TA-q_y mode [Fig. 4(c)]. The mirror symmetry of the (111) surface is broken by the transverse phonons except for the displacement parallel to the mirror plane. Hence, the mirror symmetry ($\bar{M}_i$-$\bar{\Gamma}$-$\bar{M}_i$, $i = 1,2,3$) is destroyed by TA-q_x

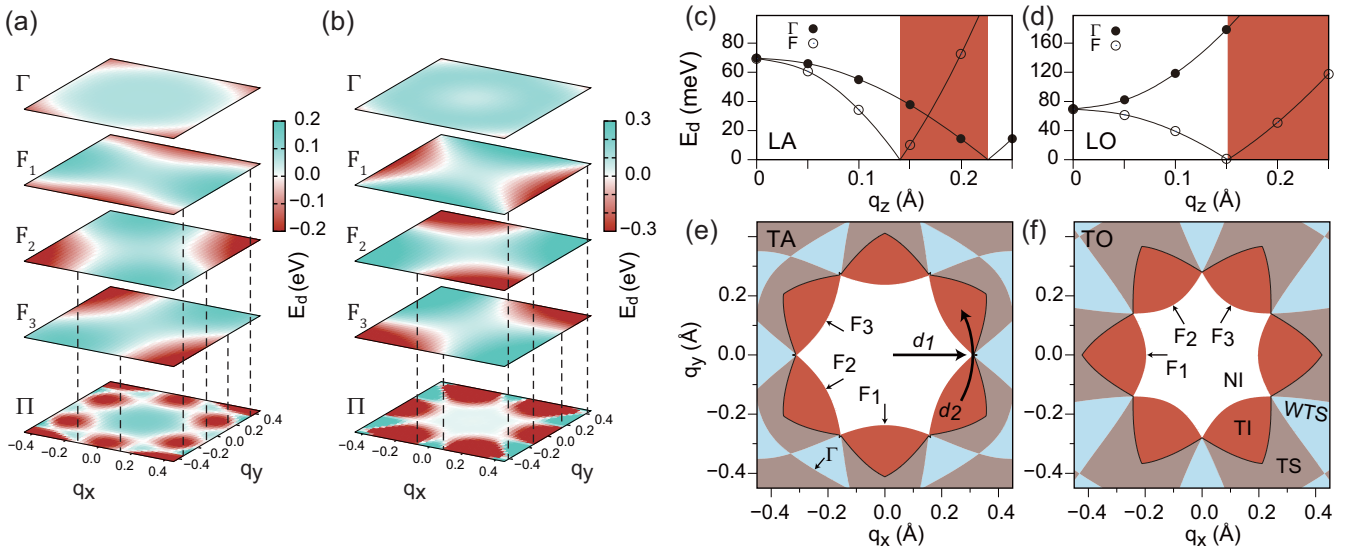

FIG. 5. (Color online) (a), (b) Calculated direct band gaps of PbS at Γ and F_i($i = 1,2,3$) under atomic displacements corresponding to (a) TA-modes and (b) TO-modes excitation. The negative band gap (in red) represents the band inversion and parity reversal. The product of the band gap at four TRIMs is plotted in the layer Π to illustrate the band inversion or the Z_2 order. (c)–(f) Calculated band gaps and the Z_2 order upon atomic displacements by the phonon modes at L point for PbS; (c) LA, (d) LO, (e) TA, and (f) TO modes. Region in red, blue, gray, and white represents the domain of TI, weak topological semimetal (WTS), TS, and NI phase, respectively.

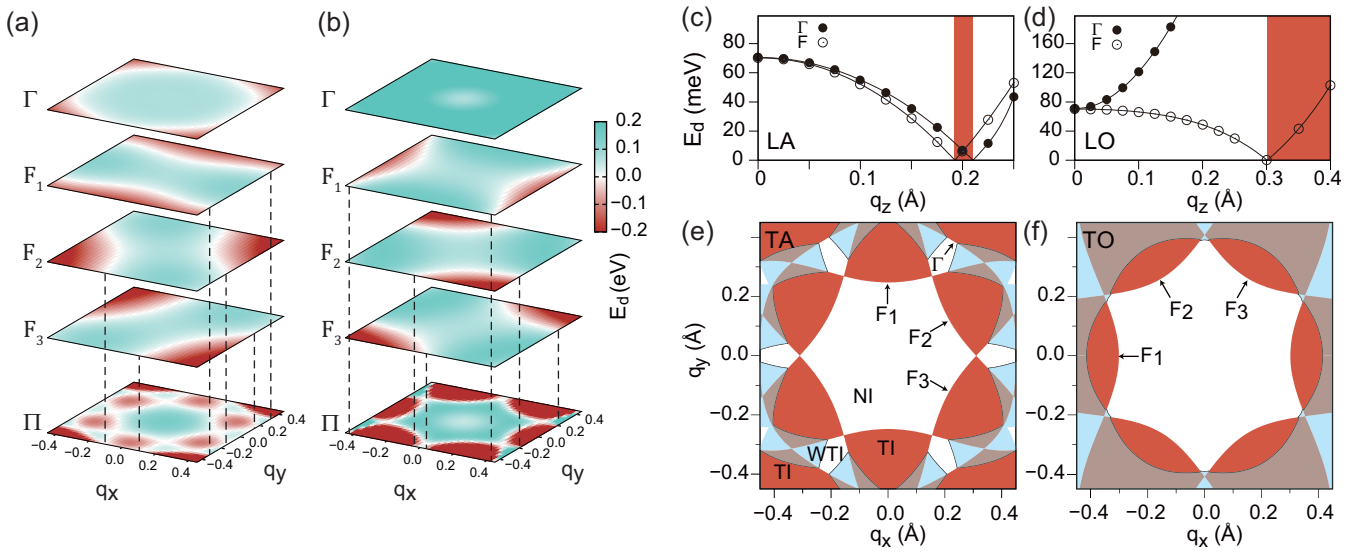

FIG. 6. (Color online) Calculated band gaps and the parity reversal upon atomic displacements by the phonon modes at L point for PbTe. (a), (b) Direct band gaps upon atomic displacements corresponding to (a) TA and (b) TO mode excitations. (c)–(f) Phase diagram of PbTe upon (c) LA, (d) LO, (e) TA, and (f) TO mode excitations.

and TO-q_x modes while the mirror symmetry along $\bar{M}_1$-$\bar{\Gamma}$-$\bar{M}_1$ survives upon TA-q_y and TO-q_y modes. We note that only TA-q_y mode (and its C_3 symmetric copies) allows the emerging Dirac cones to retain the mirror symmetry. In other words, the Dirac cones that emerge upon other transverse modes do not possess the mirror symmetry and may open the mass gap if their origin is the TCI phase. Figure 7(b), however, shows that the mass gap of the Dirac cones at $\bar{M}_2$ and $\bar{M}_3$ points does not change for the atomic displacement of ∼0.5 Å or larger even though the displacement breaks the mirror symmetry. This implies that the Dirac cones by the transverse modes are solely being protected by the time-reversal symmetry and that an even

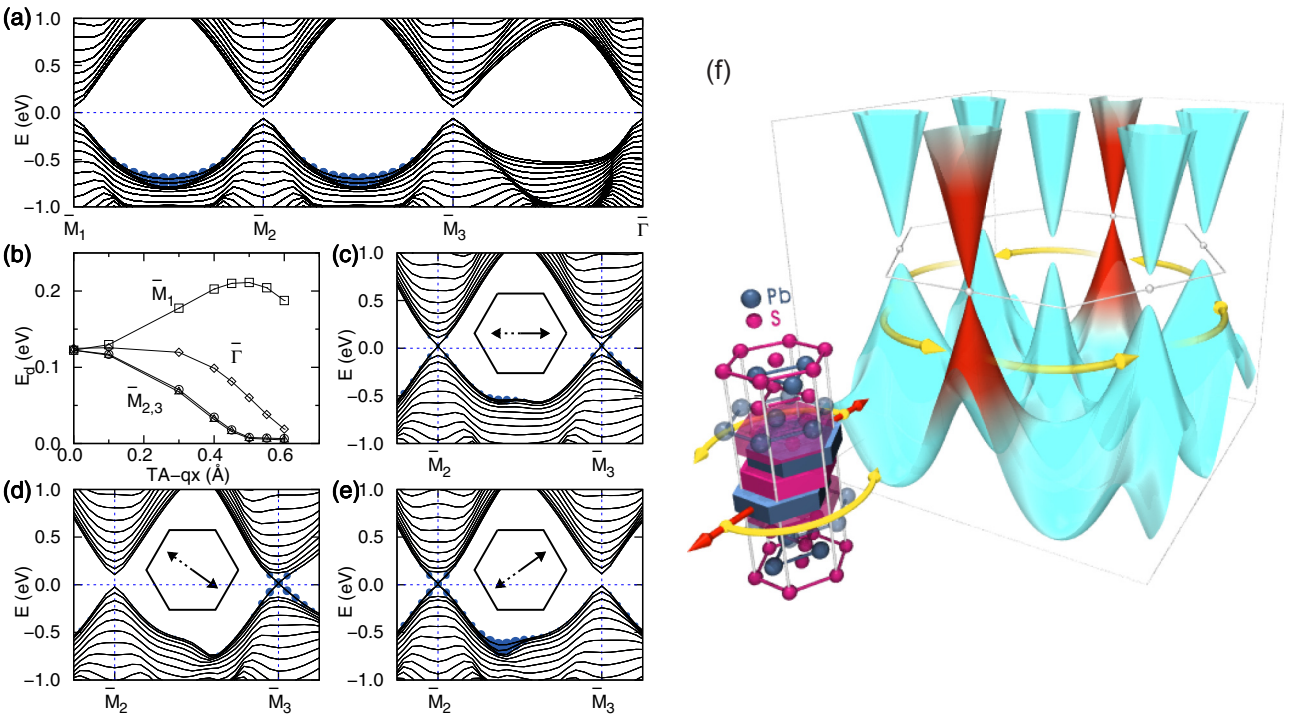

FIG. 7. (Color online) Calculated surface band structures of PbS. (a) Surface band structure without atomic displacement. (b) Direct band gaps upon atomic displacements corresponding to TA-q_x mode. (c)–(e) One or two Dirac cones are formed at $\bar{M}_i$ points for the TA mode with atomic displacement of 0.5 Å. The position of Dirac cones is determined by displacement direction of the TA mode, which is denoted in the insets [see Fig. 4(c)]. (f) Schematic view of the evolution of Dirac cones along the TRIM in the surface Brillouin zone upon the excitation of the circularly polarized TA phonon modes. The Dirac cone is formed sequentially at $\bar{M}$ points as the atomic displacement direction rotates.

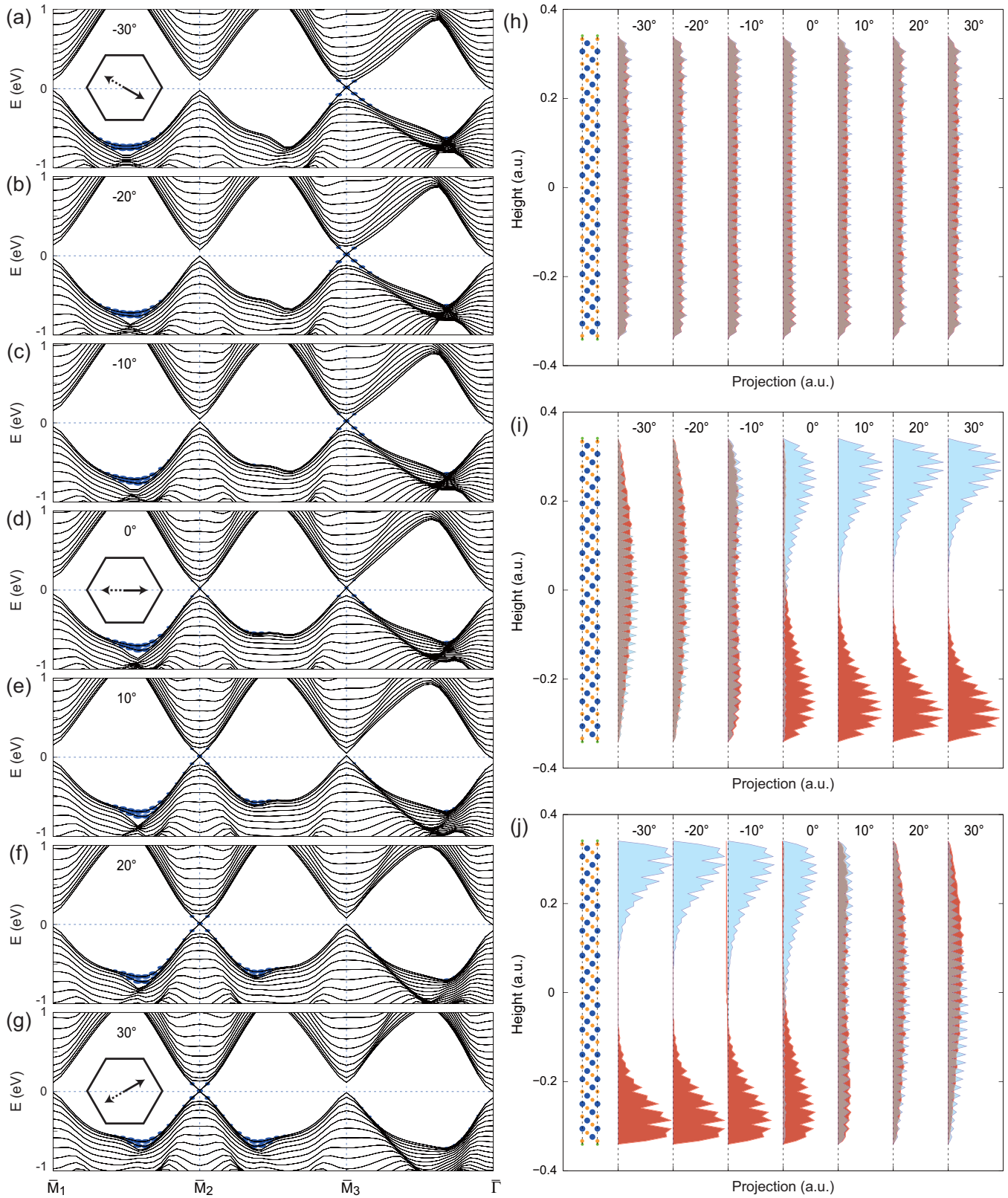

FIG. 8. (Color online) Dirac-cone dynamics during topological phase transition. (a)–(g) The evolution of the surface band structures under circularly polarized TA phonon mode corresponding to the path d_2 in Fig. 5(e). The angle in each panel is the direction of the atomic displacement from the x axis. As the atomic displacement is changed, we observe the Dirac cone emerging (vanishing) at $\bar{M}_2(\bar{M}_3)$ point. (h)–(j) The distribution of the squared wave functions for the valence-band maximum (red) and the conduction-band minimum (blue) states at (h) Γ, (i) $\bar{M}_2$, and (j) $\bar{M}_3$ points. The slab structure in the left is shown as a reference to clarify the edge localization. We observe that two wave functions are polarized to opposite surfaces when the Dirac cone appears.

number of Dirac cones that form for the weak topological order can remain intact due to distant reciprocal positions of the Dirac points. For the same reason, four Dirac cones at the (111) surface formed by the TCI phase may not open a mass gap either upon the breakdown of the mirror symmetry. A recent report [30] pointed out that the mirror symmetry works in effect only when two Dirac cones arising from the time-reversal symmetry are neutralized by mutual interactions at certain surfaces. Hence, the mass gap acquisition by the mirror-symmetry breakdown is allowed only at (001) and (011) surfaces [14], consistent with our results.

Flickering Dirac cones by lattice vibrations lead to intriguing physical consequences. For example, electrons should move back and forth to the surface to fill the Dirac cone states, producing electron-induced forces that can be utilized to control atomic migrations. The band inversion inside the bulk and emergence of the Dirac cone at surfaces occur simultaneously upon the topological phase transition. Because of the charge conservation, these two processes should take place in the same band. In other words, the band character in real space should change from bulk to surface or vice versa during the topological phase transition. As shown in Fig. 8, the flickering Dirac cones and the charge redistribution occur as the displacement of the phonon is changed; the Dirac cone at $\bar{M}_3$ point disappears from the surface to merge into the bulk states, and, at the same time, a new Dirac cone emerges from bulk at the $\bar{M}_2$ point. This indicates that the topological phase transition can exert a new type of Coulomb forces to and from the surface. Also, upon the LO phonon mode being populated, three Dirac cones will flicker simultaneously, and the electrons in each Dirac cone will oscillate between the bulk and the surface states, producing electron-dragging forces. This process can be used as a pump that transfers some spatial properties such as a magnetic moment from one surface to the other. Direct measurement of the oscillating behavior may be possible by the time-resolved spectroscopy [31,32].

IV. DISCUSSION

A major concern to realize dynamic topological phases is the large phonon energy required to generate the band inversion. Thermal energy should be ruled out as a means to excite the phonon modes over the critical amplitude because a temperature of more than $\sim$1000 K is needed. Also, all phonon modes are populated at thermal equilibrium. Disturbance by other phonons was examined by considering both acoustic and optical modes at Γ point. Acoustic phonon modes at Γ point, being equivalent to static strains, reduce or increase the band gap by the strain type while the optical modes, corresponding to dipole displacement, increase it. With all phonon modes considered, net results are summarized as the temperature coefficient of the band gap. Excitation of selective phonon modes should be done at nonequilibrium conditions using artificial tools such as piezoelectric substrates or phonon lasers. Increasing specific phonon amplitude has been explored in several ways while it may yet need more development to reach the critical value for our prediction [33–35]. A more realistic approach is to control the band gap so that the transition may occur at smaller phonon amplitudes. Chemical alloying [11,13], static strains, or hydrostatic pressure, as we showed, tune the band gap. We note that our finding of topological insulating phases in group IV-VI semiconductors by phonons can be regarded as an example of realizing the Floquet TIs, which arise from the temporal variation in trivial systems [36]. With the recent advance in experimental techniques such as femtosecond ARPES [31,32], we expect direct measurement of the topological phase transition in group IV-VI compounds by specific phonon modes to be feasible.

In summary, we studied nontrivial topological phases in group IV-VI semiconductors induced by static and dynamic lattice deformations. Topological phase transitions between TCI and NI are achieved by applying isotropic strains. By lowering the crystal symmetry to remove the degeneracy of certain TRIM, we showed that the number of band inversions can be controlled so as to induce nontrivial Z_2 topological phases in the compounds. By calculating the Z_2 invariant of the compounds by ionic displacements of selective phonon modes, we also showed that dynamic topological phases and consequently flickering surface states are realized. Our paper demonstrates that elementary excitations such as phonons can trigger the topological phases and generate intriguing transient phenomena in semiconductors.

ACKNOWLEDGMENTS

This paper was supported the SRC Center for Topological Matter (2011-0030789). The authors would like to acknowledge the support from KISTI supercomputing center through the strategic support program for supercomputing application research (No. KSC-2012-C2-68).

[1] M. Z. Hasan and C. L. Kane, Rev. Mod. Phys. **82**, 3045 (2010).
[2] X.-L. Qi and S.-C. Zhang, Rev. Mod. Phys. **83**, 1057 (2011).
[3] J. E. Moore, Nature **464**, 194 (2010).
[4] C. L. Kane and E. J. Mele, Phys. Rev. Lett. **95**, 146802 (2005).
[5] B. A. Bernevig, T. L. Hughes, and S.-C. Zhang, Science **314**, 1757 (2006).
[6] L. Fu, C. L. Kane, and E. J. Mele, Phys. Rev. Lett. **98**, 106803 (2007).
[7] L. Fu, Phys. Rev. Lett. **106**, 106802 (2011).
[8] T. H. Hsieh, H. Lin, J. Liu, W. Duan, A. Bansil, and L. Fu, Nat. Commun. **3**, 982 (2012).
[9] J. C. Y. Teo, L. Fu, and C. L. Kane, Phys. Rev. B **78**, 045426 (2008).
[10] L. Fu and C. L. Kane, Phys. Rev. Lett. **100**, 096407 (2008).
[11] S.-Y. Xu, C. Liu, N. Alidoust, M. Neupane, D. Qian, I. Belopolski, J. D. Denlinger, Y. J. Wang, H. Lin, L. A. Wray, G. Landolt, B. Slomski, J. H. Dil, A. Marcinkova, E. Morosan, Q. Gibson, R. Sankar, F. C. Chou, R. J. Cava, A. Bansil, and M. Z. Hasan, Nat. Commun. **3**, 1192 (2012).
[12] Y. Tanaka, Z. Ren, T. Sato, K. Nakayama, S. Souma, T. Takahashi, K. Segawa, and Y. Ando, Nat. Phys. **8**, 800 (2012).
[13] P. Dziawa, B. J. Kowalski, K. Dybko, R. Buczko, A. Szczerbakow, M. Szot, E. Łusakowska, T. Balasubramanian,

B. M. Wojek, M. H. Berntsen, O. Tjernberg, and T. Story, Nat. Mater. **11**, 1023 (2012).
[14] S. Safaei, P. Kacman, and R. Buczko, Phys. Rev. B **88**, 045305 (2013).
[15] G. Kresse and J. Furthmüller, Comput. Mater. Sci. **6**, 15 (1996).
[16] G. Kresse and J. Furthmüller, Phys. Rev. B **54**, 11169 (1996).
[17] J. P. Perdew, K. Burke, and M. Ernzerhof, Phys. Rev. Lett. **77**, 3865 (1996).
[18] J. Paier, M. Marsman, K. Hummer, G. Kresse, I. C. Gerber, and J. G. Angyán, J. Chem. Phys. **124**, 154709 (2006).
[19] A. V Krukau, O. A. Vydrov, A. F. Izmaylov, and G. E. Scuseria, J. Chem. Phys. **125**, 224106 (2006).
[20] P. E. Blöchl, Phys. Rev. B **50**, 17953 (1994).
[21] G. Kresse and D. Joubert, Phys. Rev. B **59**, 1758 (1999).
[22] L. Fu and C. L. Kane, Phys. Rev. B **76**, 045302 (2007).
[23] H. Lin, R. S. Markiewicz, L. A. Wray, L. Fu, M. Z. Hasan, and A. Bansil, Phys. Rev. Lett. **105**, 036404 (2010).
[24] R. Dornhaus, G. Nimtz, and B. Schlicht, *Narrow-Gap Semiconductors* (Springer-Verlag, Berlin and New York, 1983).
[25] K. Hummer, A. Grüneis, and G. Kresse, Phys. Rev. B **75**, 195211 (2007).
[26] Y.-W. Son, S.-M. Choi, Y. P. Hong, S. Woo, and S.-H. Jhi, Phys. Rev. B **84**, 155410 (2011).
[27] B. Monserrat, N. D. Drummond, and R. J. Needs, Phys. Rev. B **87**, 144302 (2013).
[28] I. Garate, Phys. Rev. Lett. **110**, 046402 (2013).
[29] K. Saha and I. Garate, Phys. Rev. B. **89**, 205103 (2014).
[30] M. Ye, J. W. Allen, and K. Sun, arXiv:1307.7191 (2013).
[31] F. Schmitt, P. S. Kirchmann, U. Bovensiepen, R. G. Moore, L. Rettig, M. Krenz, J.-H. Chu, N. Ru, L. Perfetti, D. H. Lu, M. Wolf, I. R. Fisher, and Z.-X. Shen, Science **321**, 1649 (2008).
[32] J. A. Sobota, S. Yang, J. G. Analytis, Y. L. Chen, I. R. Fisher, P. S. Kirchmann, and Z.-X. Shen, Phys. Rev. Lett. **108**, 117403 (2012).
[33] A. M. Weiner, D. E. Leaird, G. P. Wiederrecht, and K. A. Nelson, Science **247**, 1317 (1990).
[34] A. Q. Wu and X. Xu, Appl. Phys. Lett. **90**, 251111 (2007).
[35] C. A. D. Roeser, M. Kandyla, A. Mendioroz, and E. Mazur, Phys. Rev. B **70**, 212302 (2004).
[36] N. H. Lindner, G. Refael, and V. Glitski, Nat. Phys. **7**, 490 (2011).